

See discussions, stats, and author profiles for this publication at: <https://www.researchgate.net/publication/256925883>

Large Pore Donor–Acceptor Covalent Organic Frameworks

ARTICLE in CHEMICAL SCIENCE · SEPTEMBER 2013

Impact Factor: 9.21 · DOI: 10.1039/c3sc52034j

CITATIONS

17

READS

82

8 AUTHORS, INCLUDING:



Shangbin Jin

National Institute for Materials Science

21 PUBLICATIONS 418 CITATIONS

SEE PROFILE



Stephan Irle

Nagoya University

203 PUBLICATIONS 3,259 CITATIONS

SEE PROFILE



Toshikazu Nakamura

Institute for Molecular Science

153 PUBLICATIONS 7,598 CITATIONS

SEE PROFILE



Donglin Jiang

Japan Advanced Institute of Science and T...

113 PUBLICATIONS 4,899 CITATIONS

SEE PROFILE

EDGE ARTICLE

Large pore donor–acceptor covalent organic frameworks†

Cite this: *Chem. Sci.*, 2013, **4**, 4505

Shangbin Jin,^a Ko Furukawa,^b Matthew Addicoat,^c Long Chen,^{ad} Seiya Takahashi,^a Stephan Irle,^c Toshikazu Nakamura^a and Donglin Jiang^{*a}

We report the synthesis and structural characterization of large pore covalent organic frameworks (COFs) integrated with donor and acceptor building blocks. The donor and acceptor, based on triphenylene and diimide, respectively, are topologically linked to form COFs with stacked donor and acceptor columns and 5.3 nm width channels, which show high crystallinity and large surface area. By varying donor–acceptor structure in conjunction with time-resolved spectroscopy, these large-pore COFs constitute benchmark frameworks to elucidate not only the importance of donor–acceptor pairing but also the role of lattice structure in charge transfer and separation, thereby casting a general principle for the structural design of optoelectronic and photovoltaic COFs.

Received 20th July 2013

Accepted 23rd September 2013

DOI: 10.1039/c3sc52034j

www.rsc.org/chemicalscience

Introduction

Covalent organic frameworks (COFs) are a class of crystalline porous polymers that enable the elaborate integration of organic building blocks into ordered structures with atomic precision.¹ Recent advancement in the exploration of building blocks has shown the great potential of COFs for developing precise lattice structures with permanent pores.^{1–49} However, the pore size of COFs is largely restricted within 2–5 nm. The state-of-the-art large pore for hexagonal COFs is 4.7 nm,²⁹ whereas the largest pore for tetragonal COFs is 3.8 nm.³⁷ The expansion of lattice size is an important subject but it remains a synthetic challenge.^{50,51}

Here we report the synthesis and characterization of highly crystalline donor–acceptor COFs with pore size as large as 5.3 nm. We utilized triphenylene as vertices and diimide as edge units for the construction of hexagonal triphenylene–diimide COFs, which achieve a combination of striking properties including the largest pore size, high surface area and high crystallinity. Owing to the π -stacking layer structure, the donor–acceptor COFs form periodically aligned columnar

triphenylene-on-triphenylene and diimide-on-diimide arrays, which are spatially separated far enough to confine the occurrence of photochemical events to only proximate columns. Because triphenylene and diimide serve as an electron donor–acceptor pair, these large-pore COFs are benchmark frameworks that allow the elucidation of the principle for designing donor–acceptor COFs, *i.e.*, the role of lattice structure and the importance of donor–acceptor pairing in charge transfer and separation.

Various π units such as arenes, porphyrins, phthalocyanines and thiophenes have been developed for the synthesis of COFs.¹ One significant structural feature is that the COFs constitute periodically aligned π columns, which offer preorganized pathways allowing for high-rate charge carrier transport. Integration of electron donors and acceptor into the skeleton leads to the construction of donor–acceptor COFs, which consists of bicontinuously segregated and topologically aligned donor and acceptor columns.^{34,42} Such an ordered structure provides exceptionally large heterojunctions between donor and acceptor columns, which are not available by other porous or polymeric materials. The donor–acceptor heterojunction is a key structure in current technologies, including transistors, light-emitting diodes and photovoltaics, because it controls the charge dynamics in the devices. In this context, the elucidation of the principle for designing donor–acceptor COFs is of particular importance.

Results and discussion

COF synthesis and characterization

The newly synthesized large-pore donor–acceptor COFs consist of triphenylene as electron donor at vertices and naphthalene diimide or pyromellitic diimide as acceptors on edges, which

^aDepartment of Materials Molecular Science, Institute for Molecular Science, National Institutes of Natural Sciences, 5-1 Higashi-yama, Myodai-ji, Okazaki 444-8787, Japan. E-mail: jiang@ims.ac.jp

^bInstitute for Research Promotion Center for Instrumental Analysis, Niigata University, 8050 Ikarashi, 2 Nocho, Niigata 950-2181, Japan

^cWPI-Research Initiative-Institute of Transformative Bio-Molecules and Department of Chemistry, Graduate School of Science, Nagoya University, Furo-cho, Chikusa-ku, Nagoya 464-8602, Japan

^dCollege of Materials Science and Engineering, Beijing Institute of Technology, Zhongguancun South Street 5, Beijing 100081, P. R. China

† Electronic supplementary information (ESI) available: Materials and methods, synthetic procedures, Scheme S1, Tables S1–S4, Fig. S1–S7. See DOI: 10.1039/c3sc52034j

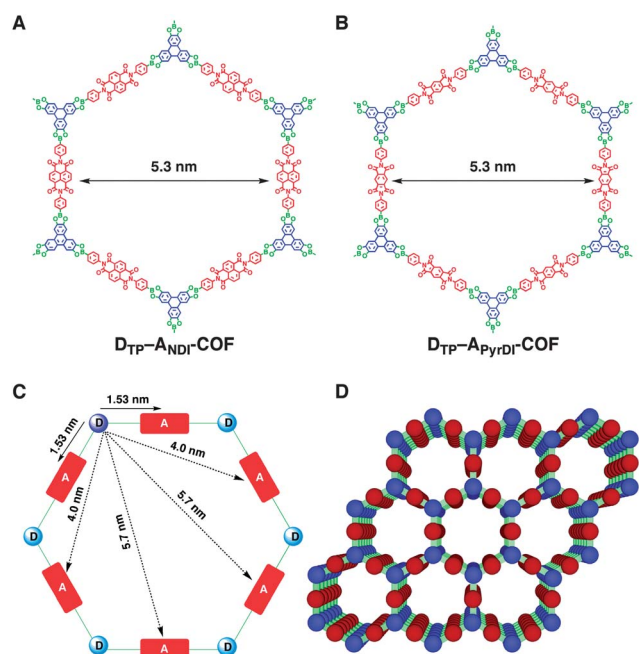
are covalently linked in a 2D hexagonal COF with a pore size of 5.3 nm (Scheme 1, $D_{TP-A_{NDI}}\text{-COF}$ and $D_{TP-A_{PyDI}}\text{-COF}$). We notice that this pore size is the largest one among COFs thus far reported.^{29,37} $D_{TP-A_{NDI}}\text{-COF}$ and $D_{TP-A_{PyDI}}\text{-COF}$ were synthesized from the reaction of 2,3,6,7,10,11-hexahydroxytriphenylene (HTTP) with *N,N'*-di-(4-boronophenyl)naphthalene-1,4,5,8-tetracarboxylic acid diimide (NDIDA) or *N,N'*-di(4-boronophenyl)pyromellitic-1,2,4,5-tetracarboxylic acid diimide (PyrDIDA), respectively, under solvothermal conditions. In a typical protocol, a mixture of monomers and solvent in a 10 mL Pyrex tube was degassed and sealed under vacuum. The tube was stand in an oven at 120 °C for 7 days. The precipitate was collected by centrifuge, washed with solvents, and dried under vacuum to yield $D_{TP-A_{NDI}}\text{-COF}$ and $D_{TP-A_{PyDI}}\text{-COF}$.

To prepare highly crystalline COFs, we performed the above reaction in different solvent mixtures including DMAc/*o*-DCB, DMAc/mesitylene, DMF/mesitylene, DMAc/toluene and DMF/toluene (Fig. S1, ESI†). Among these solvents, a mixed solvent of DMF/mesitylene (1/1 by volume) resulted in $D_{TP-A_{NDI}}\text{-COF}$ with the highest crystallinity as indicated by its intense peak in X-ray diffraction (XRD) profiles (Fig. S1, ESI†). On the other hand, the best crystallinity of $D_{TP-A_{PyDI}}\text{-COF}$ was obtained from the reaction in a mixed solvent of DMAc/*o*-DCB (1 : 1 by volume) (Fig. S2, ESI†). The solvents also have a clear effect on the porosity of COFs. For example, $D_{TP-A_{NDI}}\text{-COF}$ exhibited an increase in its Brunauer–Emmett–Teller (BET) surface area from 822 to 1009, 1193, 1385 and 1504 m² g^{−1}, respectively, as the solvent changed from DMF/toluene to DMAc/toluene, DMAc/*o*-DCB, DMF/mesitylene and DMAc/mesitylene (Table S1, ESI†). Meanwhile, the pore volume increased from 1.02 to 1.23, 1.53,

1.57 and 1.83 cm³ g^{−1}, in a same order as the BET surface area. By finely tuning reaction conditions, the BET surface area of $D_{TP-A_{PyDI}}\text{-COF}$ can reach 1910 m² g^{−1}, giving rise to a Langmuir surface area as large as 2699 m² g^{−1}, whereas the pore volume is increased to even 2.37 cm³ g^{−1}. One may notice that the hexagonal COF with a 4.7 nm pore size has a BET surface area of only 930 m² g^{−1}. $D_{TP-A_{PyDI}}\text{-COF}$ also showed a reaction solvent-dependent porosity (Table S1, ESI†). The BET surface area increased from 543 to 1263 and 1604 m² g^{−1}, respectively, as the solvent was changed from DMAc/mesitylene to DMF/mesitylene, and DMAc/*o*-DCB. The pore volume increased from 1.12 to 1.61 and 1.98 cm³ g^{−1}, which is in a same order as the BET surface area. Both $D_{TP-A_{NDI}}\text{-COF}$ and $D_{TP-A_{PyDI}}\text{-COF}$ with the highest crystallinity exhibited top level BET surface area and pore volume, among the samples.

To confirm the formation of boronate linkages between donor and acceptor units in the COFs, infrared spectroscopy was performed. Both $D_{TP-A_{NDI}}\text{-COF}$ and $D_{TP-A_{PyDI}}\text{-COF}$ exhibited clear bands at 1347 and 1063 cm^{−1}, which are assigned to the B–O and C–B bonds, respectively (Fig. S3, ESI†). Elemental analysis showed that $D_{TP-A_{NDI}}\text{-COF}$ consists of 67.55% C, 3.91% N and 3.39% H, whereas $D_{TP-A_{PyDI}}\text{-COF}$ contains 61.35% C, 4.82% N and 2.88% H; these contents agree well with theoretical values for their infinite 2D polygon sheets (ESI†). The COFs are thermally stable up to 400 °C (Fig. S4, ESI†).

Field emission scanning electron microscopy (FE-SEM) revealed that $D_{TP-A_{NDI}}\text{-COF}$ has a cubic morphology with an average size of about 200 nm (Fig. 1A), whereas $D_{TP-A_{PyDI}}\text{-COF}$ displays a needle like morphology with average size of about 300 nm (Fig. 1C). For each COF, its shape is similar and its size is quite homogeneous in the mesoscopic range. From the high-resolution transmission electron microscopic images (HR-TEM), the porous textures of $D_{TP-A_{NDI}}\text{-COF}$ and $D_{TP-A_{PyDI}}\text{-COF}$ can be clearly identified (Fig. 1B and D). These microscopic



Scheme 1 Schematic representation of structures of (A) $D_{TP-A_{NDI}}\text{-COF}$ and (B) $D_{TP-A_{PyDI}}\text{-COF}$. Dotted lines at the periphery indicate extended structure. (C) Center-to-center distances from a donor to acceptors in the COF. (D) A graphic view of a 3 × 3 porous framework.

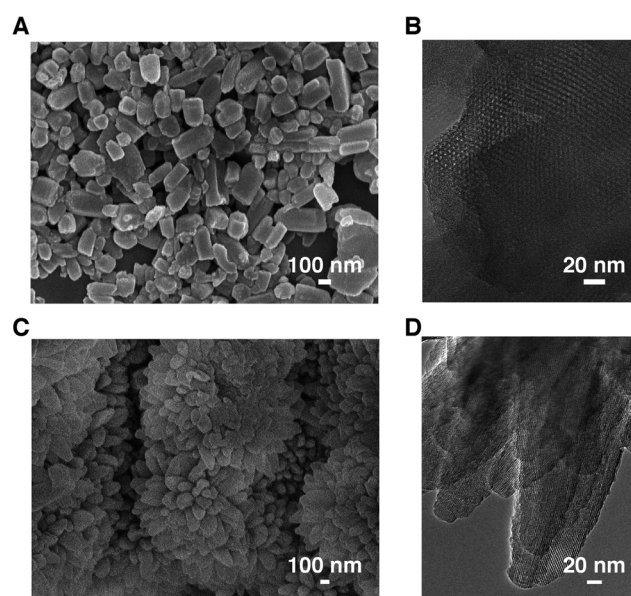


Fig. 1 FE-SEM images of (A) $D_{TP-A_{NDI}}\text{-COF}$ and (C) $D_{TP-A_{PyDI}}\text{-COF}$ and HR-TEM images of (B) $D_{TP-A_{NDI}}\text{-COF}$ and (D) $D_{TP-A_{PyDI}}\text{-COF}$.

results indicate that the polycondensation gives rise to highly porous and ordered mesoscopic materials with topologically linked hexagonal texture.

Porosity study

To characterize their porosity, nitrogen sorption isotherm curves were measured at 77 K. Both $D_{TP-A_{NDI}}-COF$ and $D_{TP-A_{PyrDI}}-COF$ displayed typical type IV sorption patterns, which are characteristic of mesoporous materials (Fig. 2A and B). As described above, they possess high surface areas and large pore volumes (Table S1, ESI†). Their pore size was calculated by using nonlocal density functional theory (NLDFT) method. Although $D_{TP-A_{NDI}}-COF$ and $D_{TP-A_{PyrDI}}-COF$ are different in acceptor structure, they have same pore size of 5.3 nm (Fig. 2B and D), which is in good agreement with their theoretical values. Most importantly, pore size distribution profiles reveal that they consist of only one kind of mesopores that account for porosity.

Crystalline structural analysis

To resolve the crystalline structure, we employed a combination of techniques including (1) Pawley refinement to confirm the XRD peak assignment, (2) density-functional tight-binding (DFTB) calculations to produce optimal structure of layered unit cell and (3) utilization of the optimal unit cell to reconstruct the XRD pattern and to establish the lattice structure. $D_{TP-A_{NDI}}-COF$ exhibited an intense XRD pattern, with clear peaks appearing at 2θ 1.92, 3.38, 3.9, 5.23, 6.84, 7.58, 9.23 and 25.3° , which are assignable to (100), (110), (200), (300), (400), (500), (600) and (001) facets, respectively (Fig. 3A, red curve). The appearance of 8 sets of XRD peaks up to the (600) facet is unprecedented for COFs and indicates an extremely high crystallinity. Similarly, $D_{TP-A_{PyrDI}}-COF$ gives sharp XRD signals at 2θ of 1.96, 3.46, 4.00, 5.30, 6.96, 8.76, 10.54 and 25.3° , which are assignable to (100), (110), (200), (300), (400), (500), (600) and (001) facets,

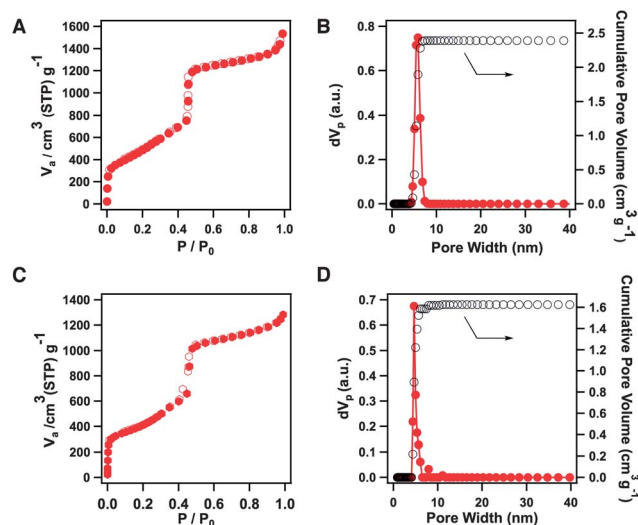


Fig. 2 Nitrogen sorption isotherm curves of (A) $D_{TP-A_{NDI}}-COF$ and (C) $D_{TP-A_{PyrDI}}-COF$, and pore size distribution of (B) $D_{TP-A_{NDI}}-COF$ and (D) $D_{TP-A_{PyrDI}}-COF$.

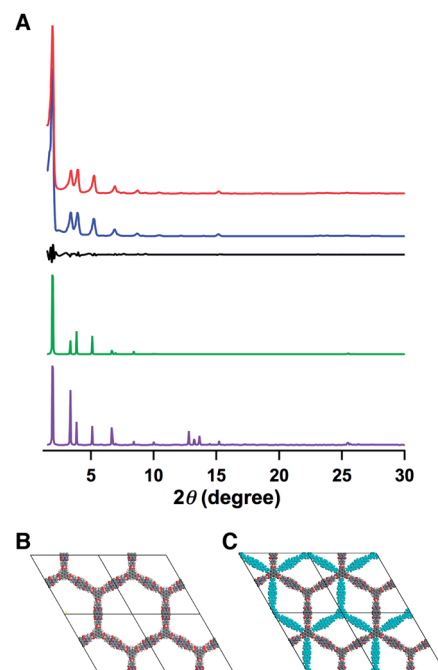


Fig. 3 XRD profiles of $D_{TP-A_{NDI}}-COF$, observed XRD patterns (red) and simulated profiles using Pawley refinement (blue) and their difference (black), 0.8 Å slipped AA stacking, (green), and staggered AB stacking (purple) modes, respectively. (B) Unit cell of 0.8 Å slipped AA stacking mode. (C) Unit cell of staggered AB stacking mode.

respectively (Fig. 4A, red curve). For both COFs, Pawley refinement using $P6/mmm$ space group yield XRD patterns (Fig. 3A and 4A, blue curves) that can reproduce the experimentally observed curves with negligible differences (Fig. 3A and 4A, black curves). This result confirmed the correctness of above assignment of XRD peaks.

The optimal unit cell structures of stacked isomers in the COFs were calculated using DFTB method including Lennard-Jones (LJ) dispersion. The single layer model system gives optimal lattice constants of $a = b = 53.0$ Å for $D_{TP-A_{NDI}}-COF$ and $a = b = 52.2$ Å for $D_{TP-A_{PyrDI}}-COF$, respectively. For each COF, three different stacking configurations, *i.e.* eclipsed AA, 0.8 Å slipped AA, and staggered AB modes were then optimized. The third dimension of the lattice, c was initialized at 3.5 Å for all structures. As shown in Table S2,† for $D_{TP-A_{NDI}}-COF$, the 0.8 Å slipped AA mode has a total crystal stacking energy of 172.56 kcal mol $^{-1}$ per unit cell, which is higher than that of eclipsed AA mode (160.21 kcal mol $^{-1}$) and much larger than that of the staggered AB mode (43.60 kcal mol $^{-1}$). For the 0.8 Å slipped AA mode of $D_{TP-A_{NDI}}-COF$, the c value converges at 3.39 Å. For $D_{TP-A_{PyrDI}}-COF$, the 0.8 Å slipped AA mode has a total crystal stacking energy of 150.97 kcal mol $^{-1}$, which is higher than that of the eclipsed AA mode (140.42 kcal mol $^{-1}$) and also much larger than that of the staggered AB mode (42.04 kcal mol $^{-1}$) (Table S2, ESI†). Therefore, for both COFs, the slipped AA stacking mode is superior to either eclipsed AA or staggered AB stacking mode.

Based on the above optimal 0.8 Å slipped AA stacking structures, we employed the Reflex Plus module of the Materials Studio for construction of unit cells with parameters of $\alpha = \beta =$

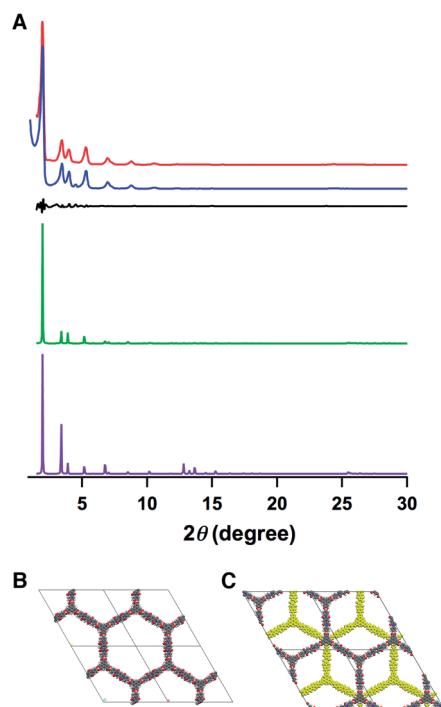


Fig. 4 XRD profiles of $D_{TP-A_{PyrDI}}COF$, observed XRD pattern (blue) and simulated profiles using Pawley refinement (red) and their difference (black), 0.8 Å slipped AA stacking (green blue), and staggered AB stacking (purple) modes, respectively. (B) Unit cell of 0.8 Å slipped AA stacking mode. (C) Unit cell of staggered AB stacking mode.

120, $\gamma = 90^\circ$, $a = b = 53.0$ Å and $c = 3.4$ Å. These unit cell parameters were utilized for the generation of lattice structure and to reconstruct XRD patterns. As shown in Fig. 3A and 4A, the simulated XRD patterns (green curves) reproduced the experimentally observed curves. In this case, the donor and acceptor units are superimposed on themselves with a slip of half bond (0.8 Å) along a and b directions (Fig. 3B and 4B; for enlarged images see Fig. S5;† for coordinates see Tables S3 and S4, ESI†). In contrast, the AB staggered stacking models using the $P1$ space group cannot reproduce the XRD patterns (purple curves). The unit cell structures of this AB staggered mode clearly show the overlap of the pores by neighboring layers (Fig. 3C and 4C).

Charge-transfer and charge-separation events

Steady-state electronic absorption spectra are informative for detecting the formation of charge transfer complexes. For example, a simple mixture of triphenylene with naphthalene diimide or pyrromellitic diimide gives rise to a largely red-shifted band at 550 or 487 nm, respectively, clearly indicating the formation of charge transfer complexes between triphenylene and naphthalene diimide or pyrromellitic diimide (Fig. 5A and B, dotted black curves). $D_{TP-A_{PyrDI}}COF$ exhibited clear charge-transfer character (Fig. 5B, green curve). In sharp contrast, no clear charge-transfer band was observed for $D_{TP-A_{NDI}}COF$ (Fig. 5A, green curve). Therefore, it can be concluded that the topological link of donor and acceptor into covalent 2D

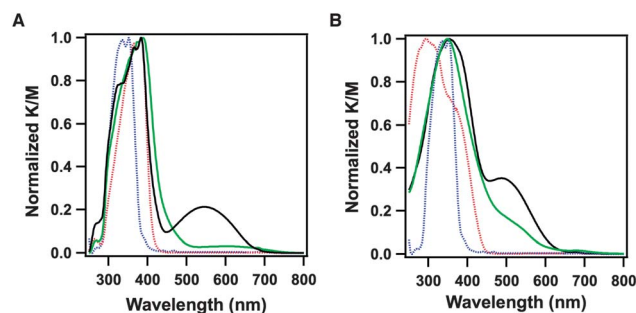


Fig. 5 Electronic absorption spectra of (A) $D_{TP-A_{NDI}}COF$ (green) and (B) $D_{TP-A_{PyrDI}}COF$ (green), simple mixtures of their monomers (black), $TP(OMe)_6$ (dotted blue), and NDI boronate ester (dotted red), PyrDI boronate ester (dotted red). For structures of $TP(OMe)_6$, NDI boronate ester and PyrDI boronate ester, see Scheme S1.†

layers with slipped AA stacking mode generates periodic donor-acceptor columnar structures. Although the lattice structures are the same, $D_{TP-A_{PyrDI}}COF$ forms a through-bond charge transfer complex, whereas in $D_{TP-A_{NDI}}COF$ the donor and acceptor columns are independent at the ground state, giving rise to a neutral system ready for charge separation. $D_{TP-A_{PyrDI}}COF$ represents a new type of charge-transfer COF with donor and acceptor covalently linked in the skeletons.

To quantitatively evaluate the lifetime of charge-separated state, we utilized time resolved electron spin resonance spectroscopy (TR-ESR) to track the formation of radical spins and their dynamics. Before the laser irradiation at 355 nm (2 mJ), the ESR signals were silent over the entire magnetic field of 0.336–0.356 T (Fig. 6A). After the laser flash, the TR-ESR signal of $D_{TP-A_{NDI}}COF$ increased rapidly in intensity up to 2.5 μ s, as the result of charge separation. We monitored magnetic field-dependent ESR spectra of $D_{TP-A_{NDI}}COF$ at 2.5 μ s, and obtained time-sliced ESR profiles (Fig. 6B). The profiles are characteristic of a single emission-type Lorentzian, which give a g value of 2.0083, which corresponds to the formation of organic radical species. The narrow spectral width of 1.51 mT (Fig. 6B, red curve) supports that there is only a weak magnetic dipolar interaction between two radical spins, which are spatially separated in donor and acceptor columns.⁴² We further monitored the ESR spectra as a function of time at the magnetic field and obtained the time profiles (Fig. 6C). An exponential function as given by $\Phi = \alpha \exp[-t/\tau_{CS}]$, whereas α , t and τ_{CS} are the proportional factor, time, and lifetime, respectively, can reproduce the time profiles. The τ_{CS} value was evaluated to be 2 μ s (Fig. 6C, sky blue curve).

In contrast to $D_{TP-A_{NDI}}COF$, $D_{TP-A_{PyrDI}}COF$ did not show any signals in the TR-ESR measurements under otherwise identical conditions (Fig. S6, ESI†). This may originate from two effects of the acceptor structure; (1) the formation of a charge-transfer complex makes the forward electron transfer less effective and (2) pyrromellitic diimide is a weaker electron acceptor than naphthalene diimide. These observations indicate that pairing donor and acceptor plays a vital role in forming charge-separation states in COFs, a key process to achieve photoenergy conversion.

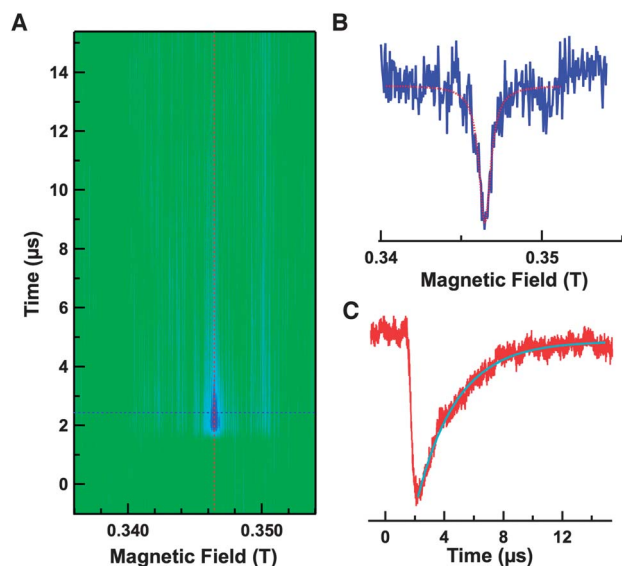


Fig. 6 (A) Contour plots of the TR-ESR spectrum of the solid-state $D_{TP-ANDI}$ -COF at 80 K. The transverse and longitudinal axes denote the time and magnetic field, respectively. The normal axis is the TR-ESR intensity. The negative and positive signs of the signal intensity indicate the absorption and emission of the micro-waves, respectively. (B) Time-slice of the TR-ESR spectrum at a time of 2.5 μ s. The red line is the line calculated based on the Lorentz function. (C) Time profile of the TR-ESR signal at a magnetic field of 0.3464 T. The sky-blue line is the curve calculated based on the exponential function $\Phi = \alpha \exp[-t/\tau_{CS}]$.

We measured the fluorescence lifetime of $D_{TP-ANDI}$ -COF by using time-resolved fluorescence spectroscopy. Fig. 7 shows the decay curves. The lifetime (τ_0) of the singlet excited state is as long as 5.23 ns for COF-10,⁴ which has no electron acceptor edge units in the framework. In sharp contrast, $D_{TP-ANDI}$ -COF has a significantly shortened lifetime (τ) of only 0.82 ns (Fig. 7A, red curve). This big difference in lifetime confirms the occurrence of photoinduced electron transfer from the triphenylene column to the proximate acceptor columns in $D_{TP-ANDI}$ -COF. From these lifetimes, the rate constant of the electron transfer (k_{ET}) was estimated using $k_{ET} = 1/\tau - 1/\tau_0$ to be $1.02 \times 10^9 \text{ s}^{-1}$, whereas the charge-separation efficiency (ϕ) was evaluated by

using an equation $\phi = 1 - \tau/\tau_0$ to be 84%. On the other hand, in $D_{TP-APyDI}$ -COF, the lifetime was evaluated as 1.0 ns (Fig. 7B, green curve), which can be attributed to charge transfer. A similar trend was also observed for the monomer mixtures, which exhibited shortened lifetimes in comparison with the donor monomer (Fig. S7, ESI†).

In the large-pore $D_{TP-ANDI}$ -COF and $D_{TP-APyDI}$ -COF, donor and acceptor are spatially separated in the hexagon at three different distances of 1.5, 4.0 and 5.7 nm, respectively (Scheme 1C). Among these donor-acceptor pairs at three different distances, charge transfer or separation takes place between only the proximate donor-acceptor columns (Scheme 1C, arrows).⁵² Such a topological confinement allows the elucidation of structural effects on photochemical events. As implied for lattice structural design, if the closest donor column-to-acceptor column distance keeps at the spatial limit of 2–3 nm for electron transfer, the pore size of a charge-transporting COF can be extended to be as large as 7–11 nm. Such a large lattice structure encourages the exploration of large π oligomers as building blocks.

Conclusions

We have synthesized and characterized novel mesoporous COFs with pore size of 5.3 nm, which is the largest pore of COFs thus far reported. Tuning reaction conditions allows the synthesis of COFs with high crystallinity and large surface area. The difference in charge transfer or charge separation caused by the difference in the acceptor structure indicates the importance of donor-acceptor pairing in functional design. Efficient electron transfer and charge separation observed for the large-pore charge-separating COF indicate that COFs are a useful platform for charge separation with a less limitation in the lattice size. These results offer a new guidance in designing COFs and may facilitate the development of various COFs with different donor-acceptor pairs to explore optoelectronic and photovoltaic functions.

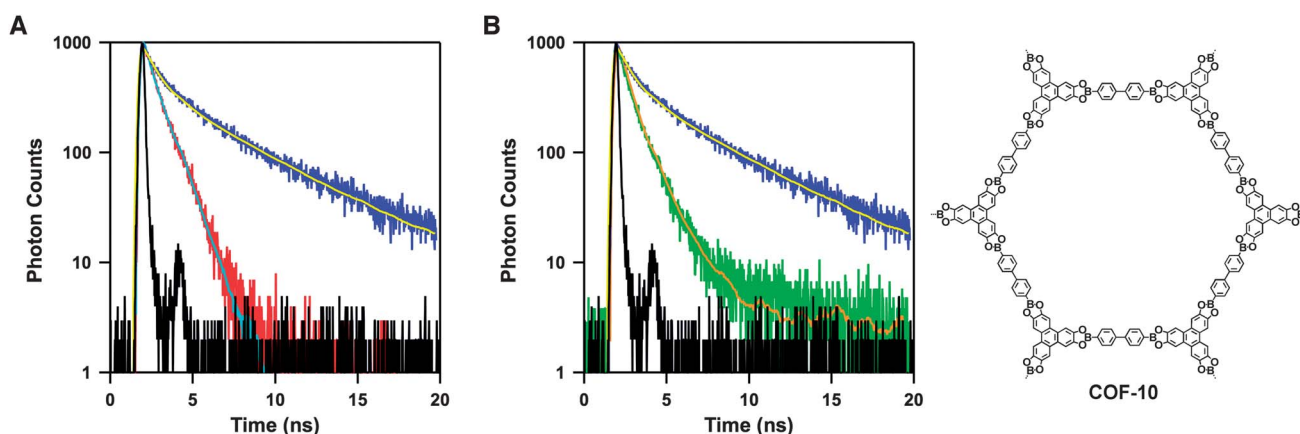


Fig. 7 Time resolved fluorescence decay profiles of $D_{TP-ANDI}$ -COF (red, sky-blue curve is a curve-fitting profile), $D_{TP-APyDI}$ -COF (green, orange curve is a curve-fitting profile) and COF-10 (blue, yellow curve is a curve-fitting profile). IRF (instrument response function) is in black.

Acknowledgements

D. J. thanks a Grant-in-Aid for Scientific Research (A) (24245030) from MEXT (Ministry of Education, Culture, Sports, Science and Technology, Japan) and partially by NSFC (Grant no. 21128001). S. I. acknowledges a CREST grant in the areas of Synthesis and Novel Functions of Soft π -Materials from JST. M. A. acknowledges the JSPS fellowship program.

Notes and references

- 1 X. Feng, X. Ding and D. Jiang, *Chem. Soc. Rev.*, 2012, **41**, 6010–6022.
- 2 A. P. Côté, A. I. Bein, N. W. Ockwig, M. O'Keeffe, A. J. Matzger and O. M. Yaghi, *Science*, 2005, **310**, 1166–1170.
- 3 R. W. Tilford, W. R. Gemmill, H. C. zur Loye and J. J. Lavigne, *Chem. Mater.*, 2006, **18**, 5296–5301.
- 4 A. P. Côté, H. M. El-Kaderi, H. Furukawa, J. R. Hunt and O. M. Yaghi, *J. Am. Chem. Soc.*, 2007, **129**, 12914–12915.
- 5 H. M. El-Kaderi, J. R. Hunt, J. L. Mendoza-Cortés, A. P. Côté, R. E. Taylor, M. O'Keeffe and O. M. Yaghi, *Science*, 2007, **316**, 268–272.
- 6 S. S. Han, H. Furukawa, O. M. Yaghi and W. A. Goddard III, *J. Am. Chem. Soc.*, 2008, **130**, 11580–11581.
- 7 J. R. Hunt, C. J. Doonan, J. D. LeVangie, A. P. Côté and O. M. Yaghi, *J. Am. Chem. Soc.*, 2008, **130**, 11872–11873.
- 8 P. Kuhn, M. Antonietti and A. Thomas, *Angew. Chem., Int. Ed.*, 2008, **47**, 3450–3453.
- 9 X. Wang, K. Maeda, A. Thomas, K. Takanabe, G. Xin, J. M. Carlsson, K. Domen and M. Antonietti, *Nat. Mater.*, 2008, **8**, 76–80.
- 10 S. Wan, J. Guo, J. Kim, H. Ihee and D. Jiang, *Angew. Chem., Int. Ed.*, 2008, **47**, 8826–8830.
- 11 R. W. Tilford, S. J. Mugavero III, P. J. Pellechia and J. J. Lavigne, *Adv. Mater.*, 2008, **20**, 2741–2746.
- 12 F. J. Uribe-Romo, J. R. Hunt, H. Furukawa, C. Klöck, M. O'Keeffe and O. M. Yaghi, *J. Am. Chem. Soc.*, 2009, **131**, 4570–4751.
- 13 H. Furukawa and O. M. Yaghi, *J. Am. Chem. Soc.*, 2009, **131**, 8875–8883.
- 14 N. L. Campbell, R. Clowes, L. K. Ritchie and A. I. Cooper, *Chem. Mater.*, 2009, **21**, 204–206.
- 15 S. Wan, J. Guo, J. Kim, H. Ihee and D. Jiang, *Angew. Chem., Int. Ed.*, 2009, **48**, 5439–5442.
- 16 C. J. Doonan, D. J. Tranchemontagne, T. G. Glover, J. H. Hunt and O. M. Yaghi, *Nat. Chem.*, 2010, **2**, 235–238.
- 17 E. L. Spitler and W. R. Dichtel, *Nat. Chem.*, 2010, **2**, 672–677.
- 18 T. Hasell, X. Wu, J. T. Jones, J. Bacsá, A. Steiner, T. Mitra, A. Trewin, D. J. Adams and A. I. Cooper, *Nat. Chem.*, 2010, **2**, 750–755.
- 19 M. J. Bojdys, J. Jeromenok, A. Thomas and M. Antonietti, *Adv. Mater.*, 2010, **22**, 2202–2205.
- 20 X. Ding, J. Guo, X. Feng, Y. Honsho, J. D. Guo, S. Seki, P. Maitarad, A. Saeki, S. Nagase and D. Jiang, *Angew. Chem., Int. Ed.*, 2011, **50**, 1289–1293.
- 21 X. Feng, L. Chen, Y. Dong and D. Jiang, *Chem. Commun.*, 2011, **47**, 1979–1981.
- 22 A. Nagai, Z. Guo, X. Feng, S. Jin, X. Chen, X. Ding and D. Jiang, *Nat. Commun.*, 2011, **2**, 536.
- 23 X. Ding, L. Chen, W. Honsho, X. Feng, O. Saengsawang, J. D. Guo, A. Saeki, S. Seki, S. Irle, S. Nagase, V. Parasuk and D. Jiang, *J. Am. Chem. Soc.*, 2011, **133**, 14510–14513.
- 24 S. Wan, F. Gandara, A. Asano, H. Furukawa, A. Saeki, S. K. Dey, L. Liao, M. W. Ambrogio, Y. Y. Botros, X. Duan, S. Seki, F. Stoddart and O. M. Yaghi, *Chem. Mater.*, 2011, **23**, 4094–4097.
- 25 F. J. Uribe-Romo, C. J. Doonan, H. Furukawa, K. Oisaki and O. M. Yaghi, *J. Am. Chem. Soc.*, 2011, **133**, 11478–11481.
- 26 L. M. Lanni, R. W. Tilford, M. Bharathy and J. J. Lavigne, *J. Am. Chem. Soc.*, 2011, **133**, 13975–13983.
- 27 J. W. Colson, A. R. Woll, A. Mukherjee, M. P. Levendorf, E. L. Spitler, V. B. Shield, M. G. Spencer, J. Park and W. R. Dichtel, *Science*, 2011, **332**, 228–231.
- 28 E. L. Spitler, M. R. Giovino, S. L. White and W. R. Dichtel, *Chem. Sci.*, 2011, **2**, 1588–1593.
- 29 E. L. Spitler, B. T. Koo, J. L. Novotney, J. W. Colson, F. J. Uribe-Romo, G. D. Gutierrez, P. Clancy and W. R. Dichtel, *J. Am. Chem. Soc.*, 2011, **133**, 19416–19421.
- 30 S. Patwardhan, A. A. Kocherzhenko, F. C. Grozema and D. A. Siebbeles, *J. Phys. Chem. C*, 2011, **115**, 11768–11772.
- 31 M. Dogru, A. Sonnnauer, A. Gavryushin, P. Knochel and T. Bein, *Chem. Commun.*, 2011, **47**, 1707–1709.
- 32 J. L. Mendoza-Cortes, W. A. Goddard III, H. Furukawa and O. M. Yaghi, *J. Phys. Chem. Lett.*, 2012, **3**, 2671–2675.
- 33 X. Feng, L. Liu, Y. Honsho, A. Saeki, S. Seki, S. Irle, Y. Dong, A. Nagai and D. Jiang, *Angew. Chem., Int. Ed.*, 2012, **51**, 2618–2622.
- 34 X. Feng, L. Chen, Y. Honsho, O. Saengsawang, L. Liu, L. Wang, A. Saeki, S. Irle, S. Seki, Y. Dong and D. Jiang, *Adv. Mater.*, 2012, **24**, 3026–3031.
- 35 X. Ding, X. Feng, A. Saeki, S. Seki, A. Nagai and D. Jiang, *Chem. Commun.*, 2012, **48**, 8952–8954.
- 36 D. N. Bunck and W. R. Dichtel, *Angew. Chem., Int. Ed.*, 2012, **51**, 1885–1889.
- 37 E. L. Spitler, J. W. Colson, F. J. Uribe-Romo, A. R. Woll, M. R. Giovino, A. Saldivar and W. R. Dichtel, *Angew. Chem., Int. Ed.*, 2012, **51**, 2623–2627.
- 38 B. T. Koo, W. R. Dichtel and P. Clancy, *J. Mater. Chem.*, 2012, **22**, 17460–17469.
- 39 S. Kandambeth, A. Mallick, B. Lukose, M. V. Mane, T. Heine and R. Banerjee, *J. Am. Chem. Soc.*, 2012, **134**, 19524–19527.
- 40 X. Feng, Y. Dong and D. Jiang, *CrystEngComm*, 2013, **15**, 1508–1511.
- 41 X. Chen, M. Addicoat, S. Irle, A. Nagai and D. Jiang, *J. Am. Chem. Soc.*, 2013, **135**, 546–549.
- 42 S. Jin, X. Ding, X. Feng, M. Supur, K. Furukawa, T. Seiya, M. Addicoat, M. E. El-Khouly, T. Nakamura, S. Irle, S. Fukuzumi, A. Nagai and D. Jiang, *Angew. Chem., Int. Ed.*, 2013, **52**, 2017–2021.
- 43 A. Nagai, X. Chen, X. Feng, X. Ding, Z. Guo and D. Jiang, *Angew. Chem., Int. Ed.*, 2013, **52**, 3770–3774.
- 44 D. N. Bunck and W. R. Dichtel, *Chem. Commun.*, 2013, **49**, 2457–2459.

- 45 M. Dogru, M. Handloser, F. Auras, T. Kunz, D. Medina, A. Hartschuh, P. Knochel and T. Bein, *Angew. Chem., Int. Ed.*, 2013, **52**, 2920–2924.
- 46 M. Dogru, A. Sonnnauer, S. Zimdars, M. Döblinger, P. Knochel and T. Bein, *CrystEngComm*, 2013, **15**, 1500–1502.
- 47 H. B. Guillaume, K. M. Vladimir, O. Ta-Chung, G. G. Robert and D. Mircea, *Proc. Natl. Acad. Sci. U. S. A.*, 2013, **110**, 4923–4928.
- 48 M. G. Rabbani, A. K. Sekizkardes, Z. Kahveci, T. E. Reich, R. Ding and H. M. El-Kaderi, *Chem.–Eur. J.*, 2013, **19**, 3324–3328.
- 49 B. P. Biswal, S. Chandra, S. Kandambeth, B. Lukose, T. Heine and R. Banerjee, *J. Am. Chem. Soc.*, 2013, **135**, 5328–5331.
- 50 D. Cao, M. Juricek, Z. J. Brown, A. C. Sue, Z. Liu, J. Lei, A. K. Blackburn, S. Grunder, A. A. Sarjeant, A. Coskun, C. Wang, O. K. Farha, J. T. Hupp and J. F. Stoddart, *Chem.–Eur. J.*, 2013, **19**, 8457–8465.
- 51 H. Deng, S. Grunder, K. E. Cordova, C. Valente, H. Furukawa, M. Hmadeh, F. Gandara, A. C. Whalley, Z. Liu, S. Asahina, H. Kazumori, M. O’Keeffe, O. Terasaki, J. F. Stoddart and O. M. Yaghi, *Science*, 2012, **336**, 1018–1023.
- 52 V. Ramamurthy and K. S. Schanze, *Organic and Inorganic Photochemistry*, Marcel Dekker, 1998.